Simulation of Dynamical Scattering Effect in Macromolecular Electron Diffraction Patterns

Tarik Drevon, David Waterman, Eugene Krissinel

21st September 2020

Contents

1 Introduction

Macromolecular structures have been successfully solved with Electron diffraction(ED) patterns and standard macromolecular X-ray crystallographic(MX) techniques since 2013 [1, 2]. This technique is currently refered to as microED. In practice, growing good quality macromolecular crystals up to micrometric sizes is often a challenge and even sometimes impossible. MicroED is therefore a very appealing technique because it enables solving structures from nanocrystals. Another interesting aspect is that ED patterns provide information about the electrostatic potential which is a complementary information to the electron density maps provided by X-ray diffraction patterns. Besides, ED patterns may provide higher resolution than the more popular cryo-EM imaging technique [3]. However, theoretical works [4, 5] have suggested that dynamical diffraction effects are too prominent for macromolecular crystals larger than a few tens of nanometer to allow the use of standard MX techniques for structure determination.

In this work, simulations of ED patterns are performed with the multislice algorithm(MS) [6, 7, 8] as an attempt to explain the discrepancies between theory and experiment.

The first section presents the MS algorithm, the second section shows an example for a 2-beam diffraction setup The third section presents simulates are performed on small molecules such as biotin.

2 Multislice algorithm

The multislice approach solves Schrodinger's equation for the incident electron beam assuming its kinetic energy is far greater than the specimen potential. This results in the real space fast electron Schrodinger's equation [8]:

$$\frac{\partial \Psi(x,y,z)}{\partial_z} = \left\{ \frac{i\lambda}{4\pi} \boldsymbol{\nabla}^2_{xy} + i\sigma V(x,y,z) \right\} \Psi(x,y,z) \tag{1}$$

where Ψ is the elctron wavefunction, $V(x,y,z)$ the specimen potential and $\sigma = 2\pi m_0 e\lambda/h^2(rad/kV\text{Å})$ the interaction parameter, λ being the relativistic electron wavelength, m_0 the electron rest mass, e the elementary charge and h plank's constant.

A direct integration along the incident beam direction z gives :

$$\Psi(z+\Delta z) = \Psi(z) \exp\left(i\lambda/4\pi\Delta z \boldsymbol{\nabla}^2_{xy}\right) \exp\left(i\sigma\nu_{\Delta z}(x,y,z)\right) \tag{2}$$

where $\nu_{\Delta_z} = \int_z^{z+\Delta z} V(x,y,z^{'})dz^{'}$ is the projected potential.

The exponentiation operator can be approximated as a propagator convolution :

$$\Psi(x,y;z+\Delta z) = p(x,y;\Delta z) * \Big(t(x,y,z)\Psi(x,y;z) \Big) + \mathcal{O}(\Delta z^2 \nu_{\Delta z}) \tag{3}$$

where $t(x,y;z) = e^{i\sigma\nu_{\Delta z}}$ is the transmission function, and $p(x,y;\Delta z) = \frac{1}{i\lambda\Delta z} e^{ik_0 \frac{x^2+y^2}{2\Delta z}}$ the Fresnel propagator.

Since convolutions can be very efficiently computed using the Fourier transform convolution theorem, the multislice algorithm is performed in practice as :

$$\Psi(x,y;z+\Delta z) \approx FFT^{-1}\left\{ P(k_x,k_y;\Delta z) FFT\Big(t(x,y;z)\Psi(x,y;z) \Big) \right\} \tag{4}$$

where $P(k_x,k_y;\Delta z) = e^{-i\pi\lambda\Delta z(k_x^2+k_y^2)}$ is the Fresnel Propagator Fourier transform, FFT and FFT^{-1} being the Fourier transform and its inverse.

In microED, the incident wave function is usually a plane wave which integrates to 1 over the transverse plane (x,y).

It is possible for reasonably small tilt angles $\theta_t \leq< 5°$[9] to simulate tilted crystals[10, 9] by using a propagator $P(k_x,k_y;\Delta z) = e^{-i\pi\lambda\Delta z(k_x^2+k_y^2)}$.

3 Application to 2-beam theory

The effect of dynamical diffraction can be demonstrated using the 2-beam configuration problem. In this configuration, 2 beams (a central beam **o** and a diffracted beam **g**) are at the Bragg condition while all other beams are far from the Bragg condition hence very weakly excited.

In 2 beam theory [11], the intensity of the non central beam should be :

$$I_{dyn-2}(S_g; t, \xi_g) = \frac{\sin^2\left(\frac{\pi t}{\xi_g}\sqrt{1+S_g^2\xi_g^2}\right)}{1+S_g^2\xi_g^2} \tag{5}$$

where $S_g(\text{Å}^{-1})$ is the excitation error i.e. the distance in reciprocal space between $q = \sin\theta/\lambda$ and the location of Bragg beam **g**. $t(\text{Å})$ is the thickness, $\xi_g = k_0/U_g$ (in Å) is the Pendellosung thickness . $k_0 = 1/\lambda$ (in Å) the incident electron wave number , $U_g = 2me/h^2 v_g(\text{in Å}^{-2})$ the structure factor and v_g (in V) the electrostaic potential Fourier components of Bragg beam **g**.

In contrast, in the kinematic case :

$$I_{kin}(S_g; t, v_g) = (\sigma v_g t)^2 \ \frac{\sin^2(\pi S_g t)}{\pi S_g t} \tag{6}$$

where $\sigma v_g = \pi/\xi_g$ so that (6) is a limit case of (5) for large ξ_g i.e. weak potential.

3.1 Simulation setup

For illustrative purposes, a simple 2D monoatomic primitive square lattice of side $a = 2$ is simulated with MS. The crystal is oriented along the [101] axis. Due to periodic boundary conditions imposed by the MS algorithm, this requires simulating a 10×10 super cell as shown in the electrostatic potential map figure 1a. The accelerated voltage is voluntary chosen at $E = 3.75keV$ to allow for Ewald sphere curvature. The configuration of the Ewald sphere is shown figure 1b where the blue dots correspond to the original reciprocal lattice rotated by $0.1rad$ from the zone axis [10] and the black dots correspond to the reciprocal lattice of the 10×10 super cell setup. The blue dots indicate miller indices $h = 0, 1, 2$ where $h = 0$ and $h = 2$ are at the Bragg condition.

The diffraction pattern is shown 2a and the major beam intensities as a function of crystal thickness are shown in figure 2b where clear oscillations appear for the excited beam pair $h = 0, 2$.

3.2 Extinction distance

The same simulation is run for different potential strengths corresponding to different atoms. A very weak potential can also be used to mimic the X-ray diffraction pattern.

In figure 3a the Beam g_1 is not at the exact Bragg condition and its intensity with crystal thickness is mostly due to Ewald sphere curvature. Indeed, the oscillation period is independent of the potential strength and mostly depends on excitation error.

On figure 3b, on the other hand, the beam for $h = 2$ is at the Bragg condition and its extinction distance is sensitive to the strength of the potential. For this strongly excited beam, dynamical diffraction is present at all potential strengths but the kinematic regime is extended to larger crystal thickness at weaker potential.

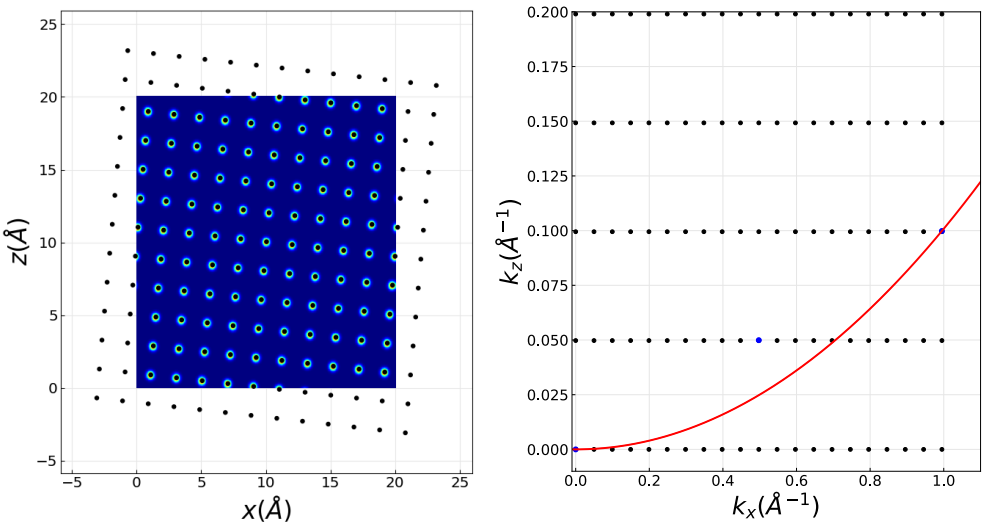

(a) (b)

Figure 1: 1a Electrostatic potential map for the 10×10 super cell (Blue area). 1b Ewald circle configuration with $E = 3.75keV$. Original reciprocal lattice (blue dots) rotated by $0.1rad$ from the zone axis [10] and reciprocal lattice of the $10x10$ super cell (black dots).

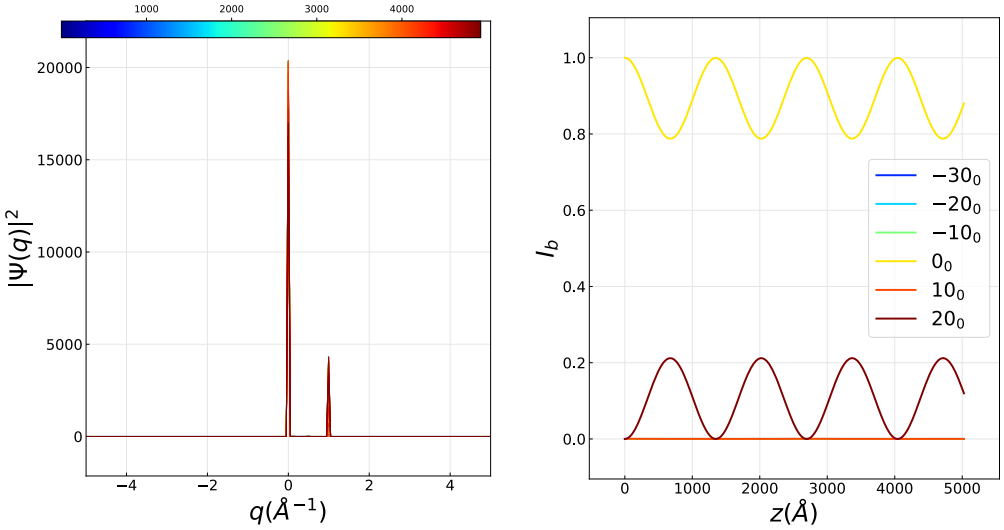

(a) (b)

Figure 2: 2a 2 beam diffraction pattern. 2b Beam intensity as function of sample thickness.

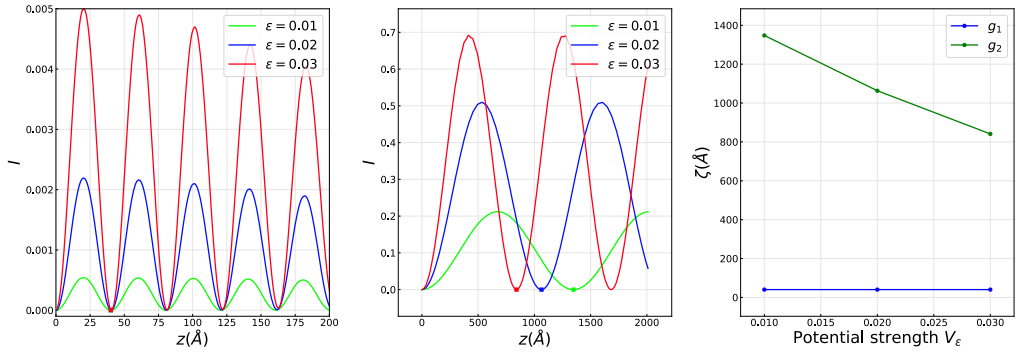

(a) (b) (c)

Figure 3: Evolution of the 3a In

3.3 Rocking curve

Rocking curves are simulated by running simulations varying the beam tilt angles from 0 to 0.08 degrees.

The actual exact Bragg condition is satisfied for the $\theta_c = 0.0385°$. At this tilt angle, the Pendullosung thickness can be measured on the $I_b(z)$ giving $\zeta_g = 293nm$. The analytical approach would give $\zeta_g = \pi/\sigma f_v(\theta_i, Z_a)$.

The rocking curves around θ_c are characteristic of 2-beam theory and shown for $z_{thick} = (0.25, 0.5, 0.75, 1, 1.25, 1.5)\,\zeta_g$.

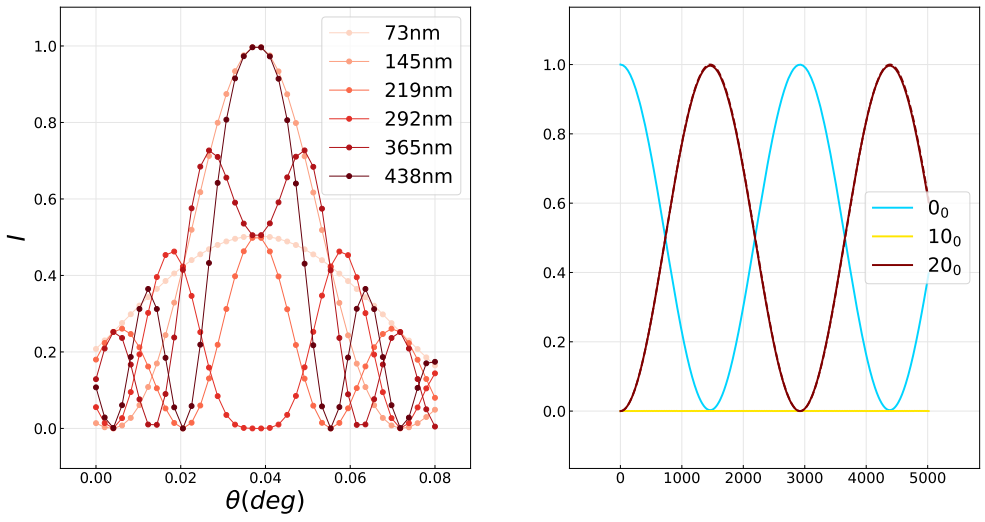

(a) (b)

Figure 4: 4 Rocking curves obtained at sample thickness $z_{thick} = (0.25, 0.5, 0.75, 1, 1.25, 1.5)\,\zeta_g$. 4b Beam intensities for $h = 0, 1, 2$ as function of sample thickness for crystal rotation $0.1 + \theta_c$ where beam $h = 2$ is at the exact Bragg condition.

4 Near Bragg : Hydrid particle-wave approach

An alternative approach to the multislice algorithm consists in solving (1) approximately using an extension of the kinematic theory to multiple scattering. This method is called near-bragg(NB) and initially developed for X-rays [**?**].

Each atom scatter the incident electron beam according to its electron-atom scattering cross section. The path length of the incident beam is computed and interference at computed at selected pixels on a detector some distance away from the sample.

4.1 Scattering by individual atoms

The first order approximation yields the kinematic theory of diffraction also known as first Born approximation. It is a perturbation treatment often used to allow for an analytical treatment. The incident state ϕ is used in place of Ψ in the right hand side so that the scattering equation can readily be solved as :

$$\Psi(\mathbf{r}) = e^{ikz} + f(\theta)\frac{e^{i\mathbf{k}\cdot\mathbf{r}}}{|\mathbf{r}|} \tag{7}$$

where :

$$f(\theta) = -\frac{2me}{h^2}\int d^3r e^{i\mathbf{q}\cdot\mathbf{r}}V(r) \quad , \quad \frac{d\sigma}{d\Omega} = |f(\theta)|^2 \tag{8}$$

where $f(\theta)$ is the scattering amplitude, i.e. the Fourier transform of the electrostatic potential. In the first Born approximation the far field diffraction pattern is proportional to the square of the scattering amplitude which is known as the differential cross section σ.

4.2 Central beam calculation

With the MS method, the intensity of the central beam corresponds to the sum of the forward scattering beam and the incident coherent unscattered beam. On the other hand, NB is based on path length calculation to compute the scattered beams contribution to the diffraction pattern. The central unscattered beam and the central forward scattered beam are therefore computed separetely. Below, the scattering cross section is used to determine the amount of unscattered beam and will be subsequently used for proper bookeeping in the implementation of double scattering.

4.2.1 Cross section, mean free path and scattering probabilities

In a continuous medium, the probability of an electron to undergo m elastic collisions and n inelastic collisions after going through a specimen of length z follows the Poisson distribution [3]:

$$P_{mn}(z) = \frac{1}{m!}\left(\frac{z}{l_e}\right)^m e^{-z/l_e}\frac{1}{n!}\left(\frac{z}{l_i}\right)^n e^{-z/l_i} \tag{9}$$

where $l_e = 1/\sigma_e\rho$ is the average elastic collision mean free path $\sigma_e = |f_a^{(e)}|^2$ being the interaction cross section and $f_a^{(e)}$ the atomic elastic scattering factor, l_i the average inelastic collision mean free path and ρ is the number of atoms per unit volume (per unit area in 2D).

For a typical protein, $\rho = 106$ atoms per nm^3, the average scattering cross section $\sigma_e = 0.001 - 0.005A^2$ (within beam energy range $E = 100 - 1000keV$) resulting in mean free path on the order of $l_e = 200 - 1000nm$. The corresponding probabilities (9)are shown figure 5. It is apparent that for the low

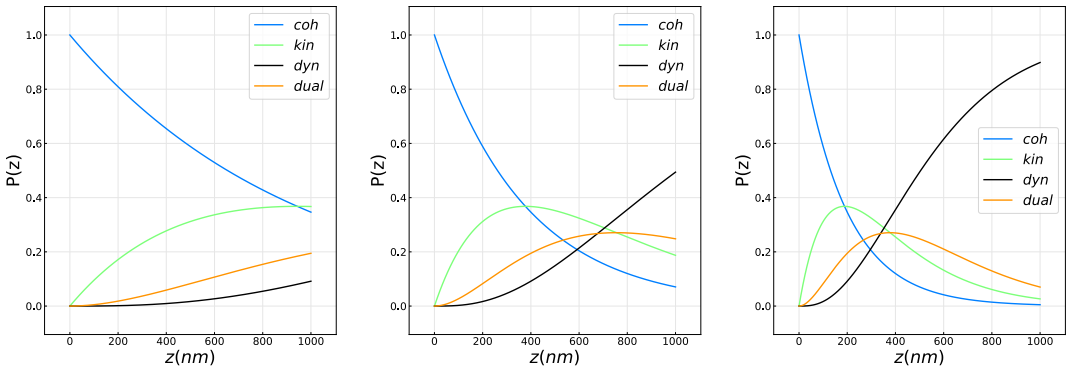

(a) (b) (c)

Figure 5: Probability of no scattering(blue), single scattering, i.e. kinematic scattering(green), double scattering(orange) and multiple scattering(solid black) as a function of crystal thickness for a typical protein crystal with average cross section and mean free path 5a $\sigma_e = 0.001\text{Å}^2$,$l_e = 943nm$, 5b $\sigma_e = 0.003\text{Å}^2$,$l_e = 377nm$, 5c $\sigma_e = 0.005\text{Å}^2$,$l_e = 188nm$.

4.2.2 Application in Near Bragg

Considering a primitive orthorombic lattice with parameters a_x b_z, a single atom per unit cell, with cross section σ_e the probability of the unscattered beam is found at cell $N+1$ from cell N as :

$$P_{N+1}^{(coh)} = P_N^{(coh)} \left(1 - \frac{dz}{l_e}\right) = P_N^{(coh)} \left(1 - \frac{\sigma_e}{a_x}\right) \tag{10}$$

where $l_e = a_x b_z/\sigma_e$ and $dz = b_z$. The solution of (10) when $dz \to 0$ results in (9) for $m = 0$.

In MS, the intensity I_0 is normalized so it integrates to unity over the transverse plane and therefore represents the density of probability of the electron. For a structure with a basis and N_x transverse unit cells, the atoms are arranged in slices of n_k atoms. The incident plane wave intensity is therefore $I_0 = 1/N_x a_x$ and the probability of an electron of being unscattered is originally $P_0^{(coh)} = 1$ and the other scattering probabilities $P_0^{(scat)} = 0$.

The fraction of electrons scattered per unit time by the array of atoms in slice k is $P_k^{(scat)} = \sum_{j=1}^{n_k} \sigma_e(j) I_0$. The number of unscattered electrons per unit time left after going through the slice k is $P_{k+1}^{(coh)} = P_k^{(coh)} - P_k^{(scat)}$ and the unscattered intensity after going through the slice is $I_0 = P_{k+1}^{(coh)}/N_x a_x$. The evolution of the probability of an electron for being unscattered at slice $k+1$ after going through slice k is therefore :

$$P_{k+1}^{(coh)} = P_k^{(coh)} \left(1 - \sum_{j=1}^{N_k} \frac{\sigma_e(j)}{N_x a_x}\right) \tag{11}$$

4.3 Kinematic calculation

In the kinematic approximation, every atom contributes once (single scattering) to the interference pattern at the detector. More precisely, the contribution of atom j to the intensity value at detector pixel i is given by the interference term $\exp(ik_0 R_{ij})/R_{ij}$ where R_{ij} is the path length

from atom j to pixel i. It is written with increasing level of approximations as :

$$R_{ij} \underset{Greens}{=} \sqrt{(x-x_0)^2+(z-z_0)^2} \tag{12}$$

$$\underset{Fresnel}{\approx} (z_0-z)+\frac{(x-x_0)^2}{2(z_0-z)} \tag{13}$$

$$\underset{Fraunhofer}{\approx} (z_0-z)+\frac{x_0^2}{2z_0}-\frac{xx_0}{z_0} \tag{14}$$

$$\tag{15}$$

where x_0, z_0 are the pixel positions and x, z are the atom position. For planar illumination, the path length from the source the to atom j is z and must be added to the path length.

The angle of scattering is determined with $\sin(\theta) = |x-x_0|/|z-z_0|$ so the atomic form factor $f(k_0 \sin(\theta))$ is used to apply the correct contribution to the scattering amplitude at that pixel.

The validity of the kinematic approximation is established by comparing NB to MS with a simple square structure with lattice constants $a_x = 10, b_z = 5$ with 100×100 unit cells. The strenght of the potential is varied to observe the onset of dynamical diffraction.

Figure 6 shows a comparison between MS and NB for a weak potential $\epsilon = 0.001$. In figure 6d, the agreement for a weak potential between the NB and MS diffraction patterns after $50nm$ propagation is good.

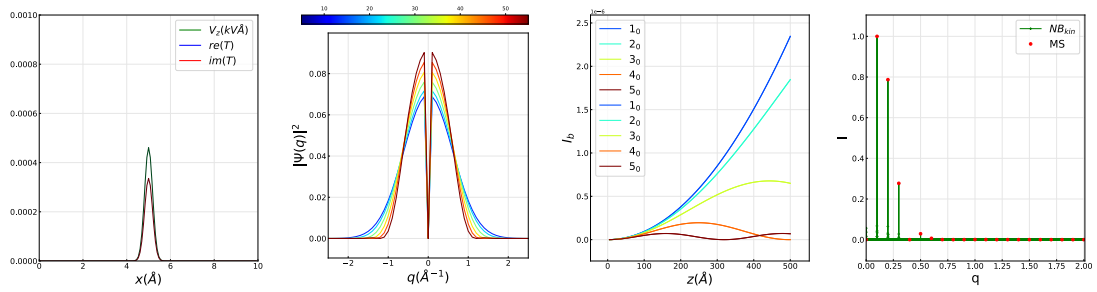

(a) (b) (c) (d)

Figure 6: 6a weak potential strength $\epsilon = 0.001$. 6b Evolution of diffraction pattern as function of thickness. 6c Evolution of major beam intensities as function of thickness. 6d comparison of diffraction patterns $t = 50nm$ for NB and MS.

Figure 7 shows on the other hand, that for a stronger potential strength $\epsilon = 0.5$, the NB kinematic approximation is not acceptable after $50nm$ propagation.

4.4 Double scattering calculation

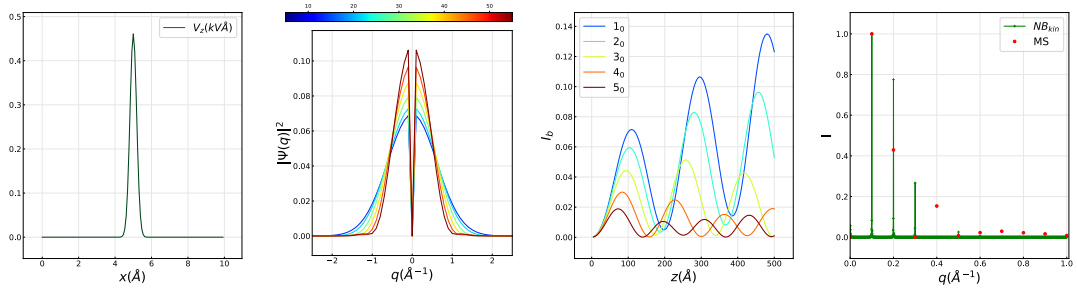

(a) (b) (c) (d)

Figure 7: 7a strong potential strength $\epsilon = 0.5$. 7b Evolution of diffraction pattern as function of thickness. 7c Evolution of major beam intensities as function of thickness. 7d comparison of diffraction patterns $t = 50nm$ for NB and MS.

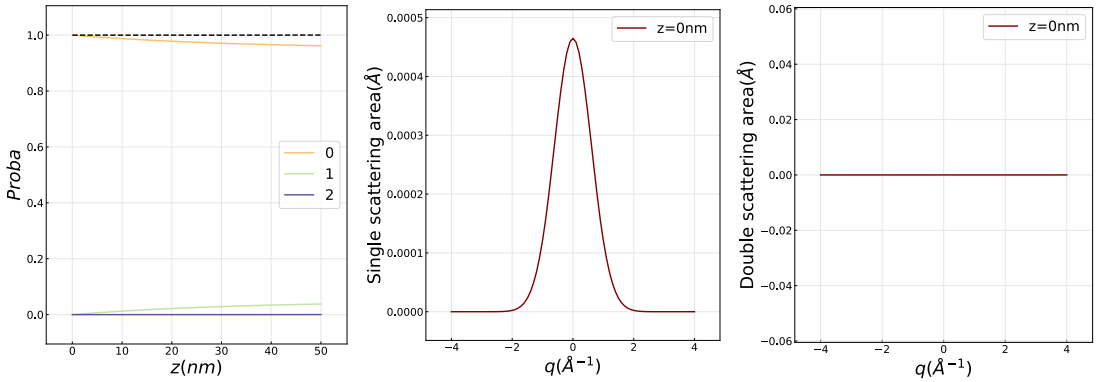

(a) (b) (c)

Figure 8: Scattering probabilities in the Near Bragg implementation 8a global, 8b single scattering distribution every 100 slices, 8c same as 8b double scattering.

References

[1] D. Shi, B. L. Nannenga, M. J. D. Cruz, J. Liu, S. Sawtelle, G. Calero, F. E. Reyes, J. Hattne, and T. Gonen, "The collection of MicroED data for macromolecular crystallography," *Nature Protoc.*, vol. 11, no. 5, pp. 895–904, 2016.

[2] M. T. Clabbers, E. V. Genderen, W. Wan, E. L. Wiegers, and T. Gruene, "Protein structure determination by electron diffraction using a single three-dimensional nanocrystal," *Acta Crystallographica Section D*, vol. 73, pp. 738–748, 2017.

[3] T. Latychevskaia and J. P. Abrahams, "Inelastic scattering and solvent scattering reduce dynamical diffraction in biological crystals," *Acta Crystallographica Section B: Structural Science, Crystal Engineering and Materials*, vol. 75, pp. 523–531, 2019.

[4] R. M. Glaeser and K. H. Downing, "High-resolution electron crystallography of protein molecules Robert," *ultramicroscopy*, vol. 52, pp. 478–486, 1993.

[5] G. Subramanian, S. Basu, H. Liu, J.-m. Zuo, and J. C. H. Spence, "Solving protein nanocrystals by cryo-EM diffraction : Multiple scattering artifacts," *Ultramicroscopy*, vol. 148, pp. 87–93, 2015.

[6] J. M. Cowley and A. F. Moodie, "The scattering of electrons by atoms and crystals. I. A new theoretical approach," *Acta Crystallographica*, vol. 10, no. 10, pp. 609–619, 1957.

[7] K. Ishizuka, "FFT Multislice Method-The Silver Anniversary," *Microscopy and Microanalysis*, vol. 10, pp. 34–40, 2004.

[8] E. J. Kirkland, *Advanced Computing in Electron Microscopy*. 2019.

[9] J. H. Chen, D. Van Dyck, and M. Op De Beeck, "Multislice Method for Large Beam Tilt with Application to HOLZ Effects in Triclinic and Monoclinic Crystals," *Acta Crystallographica Section A: Foundations of Crystallography*, vol. 53, no. 5, pp. 576–589, 1997.

[10] K. Ishizuka, "Multislice formula for inclined illumination," *Acta Crystallographica Section A*, vol. 38, no. 6, pp. 773–779, 1982.

[11] J. M. Zuo and J. C. Spence, *Advanced transmission electron microscopy: Imaging and diffraction in nanoscience*. Springer New York, jan 2016.